

# The Confinement of the Heliosheath Plasma by the Solar Magnetic Field as Revealed by Energetic Neutral Atom Simulations

M. Kornbleuth<sup>1</sup>, M. Opher<sup>1</sup>, A. T. Michael<sup>1,2</sup>, J. M. Sokół<sup>3</sup>, G. Tóth<sup>4</sup>, V. Tennishev<sup>4</sup>, J. F. Drake<sup>5</sup>

<sup>1</sup>*Astronomy Department, Boston University, Boston, MA 02215, USA*

[kmarc@bu.edu](mailto:kmarc@bu.edu)

<sup>2</sup>*Applied Physics Laboratory, Johns Hopkins University, Laurel, MD 20723, USA*

<sup>3</sup>*NAWA Bekker Fellow, Department of Astrophysical Sciences, Princeton University, Princeton, NJ 08544, USA*

<sup>4</sup>*University of Michigan, Ann Arbor, MI 48109, USA*

<sup>5</sup>*Department of Physics and the Institute for Physical Science and Technology, University of Maryland, College Park, MD, USA*

## ABSTRACT

Traditionally, the solar magnetic field has been considered to have a negligible effect in the outer regions of the heliosphere. Recent works have shown that the solar magnetic field may play a crucial role in collimating the plasma in the heliosheath. *Interstellar Boundary Explorer (IBEX)* observations of the heliotail indicated a latitudinal structure varying with energy in the energetic neutral atom (ENA) fluxes. At energies  $\sim 1$  keV, the ENA fluxes show an enhancement at low latitudes and a deficit of ENAs near the poles. At energies  $> 2.7$  keV, ENA fluxes had a deficit within low latitudes, and lobes of higher ENA flux near the poles. This ENA structure was initially interpreted to be a result of the latitudinal profile of the solar wind during solar minimum. We extend the work of Kornbleuth et al. (2018) by using solar minimum-like conditions and the recently developed SHIELD model. The SHIELD model couples the magnetohydrodynamic (MHD) plasma solution with a kinetic description of neutral hydrogen. We show that while the latitudinal profile of the solar wind during solar minimum contributes to the lobes in ENA maps, the collimation by the solar magnetic field is important in creating and shaping the two high latitude lobes of enhanced ENA flux observed by *IBEX*. This is the first work to explore the effect of the changing solar magnetic field strength on ENA maps. Our findings suggest that *IBEX* is providing the first observational evidence of the collimation of the heliosheath plasma by the solar magnetic field.

*Subject headings:* ISM: atoms - magnetohydrodynamics (MHD) - solar wind - Sun: heliosphere

## 1. Introduction

The heliosphere is created via the interaction of the solar wind plasma with the partially ionized plasma of the local interstellar medium (ISM). The solar cycle consists of a progression from solar minimum ( $\sim 400$  km/s solar wind at low latitudes,  $\sim 750$  km/s wind at high latitudes) to solar

maximum ( $\sim 400$  km/s solar wind at all latitudes) and back to solar minimum. The solar wind dynamic pressure varies as the solar wind speed and density changes in time affecting the heliospheric boundaries and the energetic neutral atom (ENA) production (McComas et al. 2018, 2019; Zirnstein et al. 2018). Additionally, the solar magnetic field intensity changes in magnitude during the course

of the solar cycle.

Traditionally, the accepted shape of the heliosphere is comet-like (Parker 1961; Baranov & Malama 1993), with a long tail extending for thousands of AU in the direction opposite ISM flow (the heliotail). Recently, this notion was challenged by models and observations. Opher et al. (2015) used a magnetohydrodynamic (MHD) simulation to propose that the magnetic tension of the solar magnetic field alters flows in the heliosheath to produce a “croissant” heliosphere with lobes directed to the north and south. This model includes a shortened heliotail, where the distance from the Sun to the tail is similar to the distance from the Sun to the nose. Dialynas et al. (2017) proposed a bubble-like heliosphere, also with a shortened heliotail, based on ENA measurements (30–55 keV) from the Ion and Neutral Camera onboard *Cassini*. One important feature of the Opher et al. (2015) model was the ability of the solar magnetic field to collimate the solar wind plasma. Pogorelov et al. (2015) and Izmodenov & Alexashov (2015, 2018) argue for a long-tail heliosphere, but show evidence of this collimation process while using a unipolar magnetic field.

Energetic Neutral Atoms (ENAs) originate as pick-up ions (PUIs) in the solar wind plasma and can provide an indirect method for studying the structural properties of the heliosphere. The *Interstellar Boundary Explorer (IBEX)* was launched 2008 October 19 to study the heliosphere by observing ENAs (McComas et al. 2009). The *IBEX-Hi* camera (Funsten et al. 2009) measures ENAs from  $\sim 300$  eV to  $\sim 6$  keV. ENA images of the heliotail by *IBEX* (McComas et al. 2013) show a multi-lobe structure. These lobes were attributed to signatures of slow and fast wind within the long heliospheric tail as part of the 11-year solar cycle. Zirnstein et al. (2016, 2017), using a time dependent simulation with solar cycle variations of the solar wind, reproduced the spectral dependence and heliotail ENA maps as shown by *IBEX* with a model of the heliotail resembling a long comet-like tail.

Kornbleuth et al. (2018) investigated the ENA maps from the “croissant” heliosphere (Opher et al. 2015) with a uniform solar wind. The collimation of the heliosheath plasma by the solar magnetic field created high latitude lobes despite the lack of fast solar wind at the poles. These

high latitude lobes persisted in all energies contrary to observations. Kornbleuth et al. (2018) included a solar magnetic field with a radial component of 6.45 nT at 1 AU, representative of solar maximum-like conditions as in Opher et al. (2015), which is higher than other models such as 3.5 nT in Pogorelov et al. (2015) and 3.75 nT in Izmodenov & Alexashov (2015). These lower values for the radial solar magnetic field component reflect the field strength seen at solar minimum.

By using a time dependent MHD solution as in Zirnstein et al. (2017), it is difficult to disentangle the effects of a latitudinally dependent solar wind and the solar magnetic field. Previous studies suggested the latitudinally dependent solar wind is responsible for the energy dependent ENA structures in the heliotail observed by *IBEX* (McComas et al. 2013; Zirnstein et al. 2016, 2017). Kornbleuth et al. (2018) suggested the solar magnetic field could play a key role in the formation of observed high latitude lobes, but only used solar maximum-like conditions. Therefore, it is critical to disentangle the effects of the solar wind structure and the solar magnetic field to understand the origin of ENAs in observations.

The purpose of this paper is to extend our previous work (Kornbleuth et al. 2018) to investigate the effect of a latitudinally-varying solar wind and the strength of the solar magnetic field. Other works, such as Ratkiewicz et al. (2012), have studied the effect of the interstellar magnetic field on ENA maps. In contrast, the work in this paper focuses on the effect of the solar magnetic field, which has often been regarded as having a negligible effect. We use conditions from the year 2008, corresponding to a period of solar minimum. We compare with the first five years of *IBEX* data that correspond to the solar minimum period. In Section 2, we discuss the model used in this work. In Section 3, we present the results of our model, focusing on the different roles of the solar wind structure and the solar magnetic field. In Section 4, we discuss the implications of our modeling.

## 2. Model

### 2.1. MHD Simulations

We use the Solar-wind with Hydrogen Ion Exchange and Large-scale Dynamics (SHIELD) model from Michael (2019) and Michael et al.

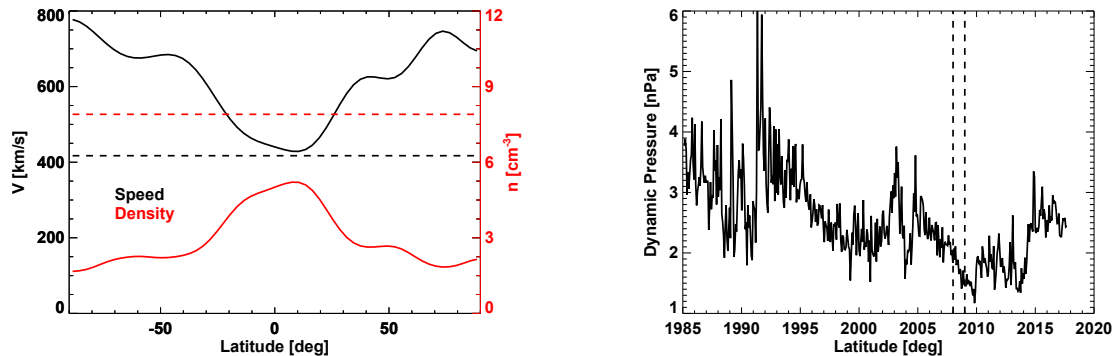


Fig. 1.— Left: Solar wind conditions at 1 AU for different heliolatitudes corresponding to the 2008-averaged solar wind data from Sokół et al. (2015) used in Cases 1 and 2 (solid) and the uniform solar wind used in Cases 3 and 4 (dashed). The black lines correspond to the solar wind speed and the red lines correspond to the solar wind density. Right: Variation of solar wind dynamic pressure with time for the equator at 1 AU from Sokół et al. (2015). The dashed vertical lines indicate the start and end of the year 2008, over which the solar wind data in Cases 1 and 2 are averaged.

(2020). This model extends the MHD solution of Opher et al. (2015) to become a global, self-consistent kinetic-MHD model of the heliosphere. The model treats the plasma as a single ion species using the MHD equations and describes the neutral hydrogen kinetically. Our model uses a Cartesian grid, with the outer boundary located at  $x = \pm 1500$  AU,  $y = \pm 2000$  AU, and  $z = \pm 2000$  AU. The neutrals flow throughout the domain, and the ISM enters the domain from the  $x = -1500$  AU face. For the ISM, we use the following parameters from Opher et al. (2020):  $n_H = 0.18 \text{ cm}^{-3}$  for the neutral hydrogen,  $n_p = 0.06 \text{ cm}^{-3}$  for the ISM protons,  $v_{ISM} = 26.4 \text{ km s}^{-1}$ ,  $T_{ISM} = 6519 \text{ K}$ , and  $B_{ISM} = 3.2 \text{ } \mu\text{G}$ . These boundaries are chosen because they give good agreement with the measurements of Voyager 1 & 2 outside of the heliopause.

Our inner boundary conditions are specified at 10 AU. We use the solar wind speed and density from Sokół et al. (2015). These authors used the solar wind speed derived from the interplanetary scintillation (IPS) observations by the Institute for Space-Earth Environmental Research at Nagoya University (Tokumaru et al. 2010, 2012). They reconstructed the spatial and temporal variation of the solar wind speed and density at 1 AU from 1985 to 2013. We use yearly-averaged solar wind

data corresponding to the year 2008 for our inner boundary conditions with  $3^\circ$  resolution in latitude and assume longitudinal symmetry (Figure 1). This year corresponds to typical solar minima conditions. We determine the solar wind temperature at 1 AU using those data and assume a Mach number of 6 at all latitudes at 1 AU. We extrapolate the solar wind conditions to 10 AU assuming the flow to be adiabatic. As in Opher et al. (2015), we treat the solar magnetic field as a unipole with the same polarity in both hemispheres to avoid artificial numerical reconnection at both the nose of the heliosphere and also in the solar magnetic equator across the heliospheric current sheet. The radial component of the solar magnetic field is set at the equator as 2.94 nT at 1 AU. This value was taken from yearly-averaged OMNI magnetic field data for the year 2008 at 1 AU. The solar magnetic field is modeled as a Parker spiral (Parker 1958).

The SHIELD model uses the Adaptive Mesh Particle Simulator (AMPS) to treat the neutral hydrogen kinetically. AMPS is a global, kinetic, 3D particle code developed within the framework of the Direct Simulation Monte Carlo methods (Tenishev et al. 2008). The multi-fluid approximation, which describes the neutrals as four separate fluids, is used to relax the plasma to a steady state solution in the MHD model, and is used to

Case	$n \text{ cm}^{-3}$	$U \text{ km/s}$	$B_r \text{ nT}$	Latitudinal Variation of Solar Wind
Case 1	5.1	437.7	0	yes
Case 2	5.1	437.7	2.94	yes
Case 3	7.9	417.1	2.94	no
Case 4	7.9	417.1	6.45	no

Table 1: The four cases used in this work. The solar wind density ( $n$ ) and speed ( $U$ ), as well as the radial component of the solar magnetic field ( $B_r$ ) are given for each case at 1 AU for the solar equator. Cases 1 and 2 represent solar minimum-like conditions with slow wind at the low latitudes and fast wind at the high latitudes. Cases 3 and 4 represent solar maximum-like conditions, with a uniform solar wind profile across all latitudes. For all cases, longitudinal symmetry is assumed.

start SHIELD. The resolution of the MHD model is  $\Delta x = 3$  AU in the supersonic solar wind (within  $x = \pm 120$  AU) and  $\Delta x = 6$  AU in the heliosheath (from  $x = -240$  AU at the nose until  $x = 560$  AU at the heliotail). The resolution of AMPS within the heliosphere is  $\Delta x = 4.7$  AU (from  $x = -280$  AU at the nose until  $x = 560$  AU at the heliotail). The SHIELD model is run in local time to cycle between the MHD model and AMPS, which allows for statistics to accumulate between each step of the plasma solution (Michael et al. 2020). Use of a local time step (Tóth et al. 2012) is appropriate for steady state solutions. Approximately 140 million particles are modeled within AMPS, and the source terms to the MHD equations due to charge-exchange with the neutral hydrogen atoms accrue for 5,000 time steps within AMPS before being passed to the MHD solver to update the plasma solution for one time step. Once the plasma solution is updated, it is passed back to AMPS. This process is repeated until a new approximate steady state solution is reached.

In order to probe the effects of a latitudinally-varying solar wind and the strength of the solar magnetic field on the solution, we run four different cases (Table 1). Cases 1 and 2 correspond to solar minimum-like conditions, while Cases 3 and 4 correspond to solar maximum-like conditions. Case 1 utilizes the yearly-averaged 2008 solar wind conditions (Figure 1) from Sokół et al. (2015); however, the solar magnetic field is not included. Case 2 includes the 2008 solar wind conditions and also the solar magnetic field. Case 3 is based on the model used in Kornbleuth et al. (2018). We use the outer boundary conditions detailed above and the same solar magnetic field as in Cases 1 and 2, but we use a uniform solar wind

profile (as in Kornbleuth et al. 2018) corresponding to solar maximum-like conditions from (Opher et al. 2015) with a density of  $n_{SW} = 7.9 \text{ cm}^{-3}$ , temperature of  $T_{SW} = 2.9 \times 10^5 \text{ K}$ , and speed of  $v_{SW} = 417.1 \text{ km/s}$  at 1 AU (Figure 1). Case 4 utilizes the same conditions as Case 3, except the radial solar magnetic field at the equator is set to be 6.45 nT at 1 AU instead of 2.94 nT. This intensity corresponds to solar maximum-like conditions used in Opher et al. (2015).

## 2.2. ENA Flux Model

We update the model of Kornbleuth et al. (2018) to account for variation in solar wind speed and density at different latitudes in the supersonic solar wind. When including the latitudinal variation of the solar wind, the speed and density of the plasma must be considered with regard to the creation of PUIs via charge exchange.

We use the PUI density fraction at the termination shock,  $\alpha$ , from Zirnststein et al. (2017), which is based on the work of Lee et al. (2009), given by

$$\alpha(\mathbf{r}_{TS}) = \frac{r_{TS}}{u_{p,1au} n_{p,1au}} n_{H,avg} (\nu_{ph,1au} + \sigma_{ex} u_{p,1au} n_{p,1au}), \quad (1)$$

where  $r_{TS}$  is the distance for the termination shock,  $u_{p,1au}$  is the speed of the solar wind at 1 AU,  $n_{p,1au}$  is the density of the solar wind at 1 AU, and  $n_{H,avg}$  is the average neutral hydrogen density between the inner boundary and the termination shock for a given direction. The term  $\nu_{ph,1au}$  is the photoionization rate at 1 AU assumed to be  $8 \times 10^{-8} \text{ s}^{-1}$  (e.g., Sokół et al. 2019). As in Zirnststein et al. (2017), we assume the constant pho-

toionization rate, although it varies in time and space. The photoionization rate contributes about 20% to the total ionization rates for hydrogen, with charge exchange being the dominant ionization process (see more, e.g., Sokół et al. 2019). Therefore our approximation does not change the conclusions. The charge-exchange cross section,  $\sigma_{ex}$ , is used from Lindsay & Stebbings (2005).

Similar to Kornbleuth et al. (2018), we include the angular dependence of PUIs in our model via

$$n_{PUI}(\mathbf{r}) = n_i(\mathbf{r}) \frac{\alpha(\theta, \phi)}{\alpha(\theta_{nose}, \phi_{nose})}, \quad (2)$$

where  $\theta$  is the polar angle, and  $\phi$  is the azimuthal angle. The polar angle increases from the northern pole toward the southern pole, while the azimuthal angle increases in the clockwise direction from the tail. The parameter  $n_i$  is the density of the PUI species for a given direction calculated using the total plasma density multiplied by the density fractions (Kornbleuth et al. 2018). We partition the plasma from the MHD solution into three populations of ions based on the work of Zank et al. (2010): solar wind ions, transmitted PUIs, and reflected PUIs, with their density ratios relative to the plasma given by 0.836, 0.151, and 0.013, respectively, and their energy ratios given by 0.04, 0.50, and 0.46, respectively. The total thermal energy of the plasma is conserved via this partitioning, given by (Zank et al. 2010)

$$T_p = \left( \frac{n_{SW}}{n_p} \Gamma_{SW} + \frac{n_{tr}}{n_p} \Gamma_{tr} + \frac{n_{ref}}{n_p} \Gamma_{ref} \right) T_p, \quad (3)$$

where  $n_p$  and  $T_p$  are the density and temperature of the plasma,  $n_i$  is the density for the respective ion population, and  $\Gamma_i$  is the temperature fraction for the respective ion population given by  $\Gamma_i = T_i/T_p$ , with  $T_i$  being the temperature for the respective ion population. We use the cold electron approximation for the plasma, where the electrons are assumed to have the same temperature as the solar wind ions. Therefore, the plasma temperature is given by (Zirnstein et al. 2017)

$$T_p = \frac{2T_{MHD}}{1 + \Gamma_{SW}}, \quad (4)$$

where  $T_{MHD}$  is the temperature given from the MHD solution. We also assume quasi-neutrality.

We are not modeling the ENA the contribution from the region in the heliotail where material with heliosheath properties sits on magnetic field lines open to the ISM (Michael et al. 2018), called “open heliosheath”. Kornbleuth et al. (2018) showed that the “open heliosheath” region could enhance the ENA flux observed in the low latitude tail. Since the purpose of this work is to focus on the effects of the solar magnetic field and the latitudinal structure of the solar wind, the exploration of the contribution of “open heliosheath” is left to a future work.

### 3. Results

In Figure 2, we present the tail-centered maps from our different cases, and tail-centered maps of *IBEX* data from the first five years (Schwadron et al. 2014). Schwadron et al. (2014) applied a mask over the region surrounding the *IBEX* ribbon in order to observe the globally distributed flux (GDF) from ENAs within the heliosheath using *IBEX* data averaged over the first five years. Similar to Zirnstein et al. (2017), we scale the ENA flux in our modeled maps by a certain factor (1.8) to match observations. Case 1, which neglects the solar magnetic field, demonstrates a stronger lower energy ENA flux at low latitudes compared to high latitudes. With increasing energy, the ENA flux at high latitudes increases relative to the ENA flux at lower latitudes. This transition is a consequence of the latitudinally-dependent solar wind profile, where ENA flux at the highest energies of *IBEX* are dominated by parent ions from the fast solar wind. At energies  $> 2$  keV, the ENA maps have two separated lobes of enhanced ENA flux. The peak flux of the northern lobe is centered at an ecliptic (longitude, latitude)  $(\lambda, \beta) = (96^\circ, 42^\circ)$  and the southern lobe has a peak flux located at  $(\lambda, \beta) = (72^\circ, -30^\circ)$  in the 2.73 keV energy band. There is also the appearance of port and starboard lobes discussed in McComas et al. (2013) and Zirnstein et al. (2016). We see these same features in Case 2, which includes the solar magnetic field, with the northern lobe having peak flux centered at  $(\lambda, \beta) = (108^\circ, 42^\circ)$  and the southern lobe having peak flux at  $(\lambda, \beta) = (78^\circ, -30^\circ)$  in the 2.73 keV energy band. The high latitude lobes at the 2.73 and 4.29 keV energy bands are significantly enhanced in size and flux relative to the case without solar magnetic field. The collimation of the so-

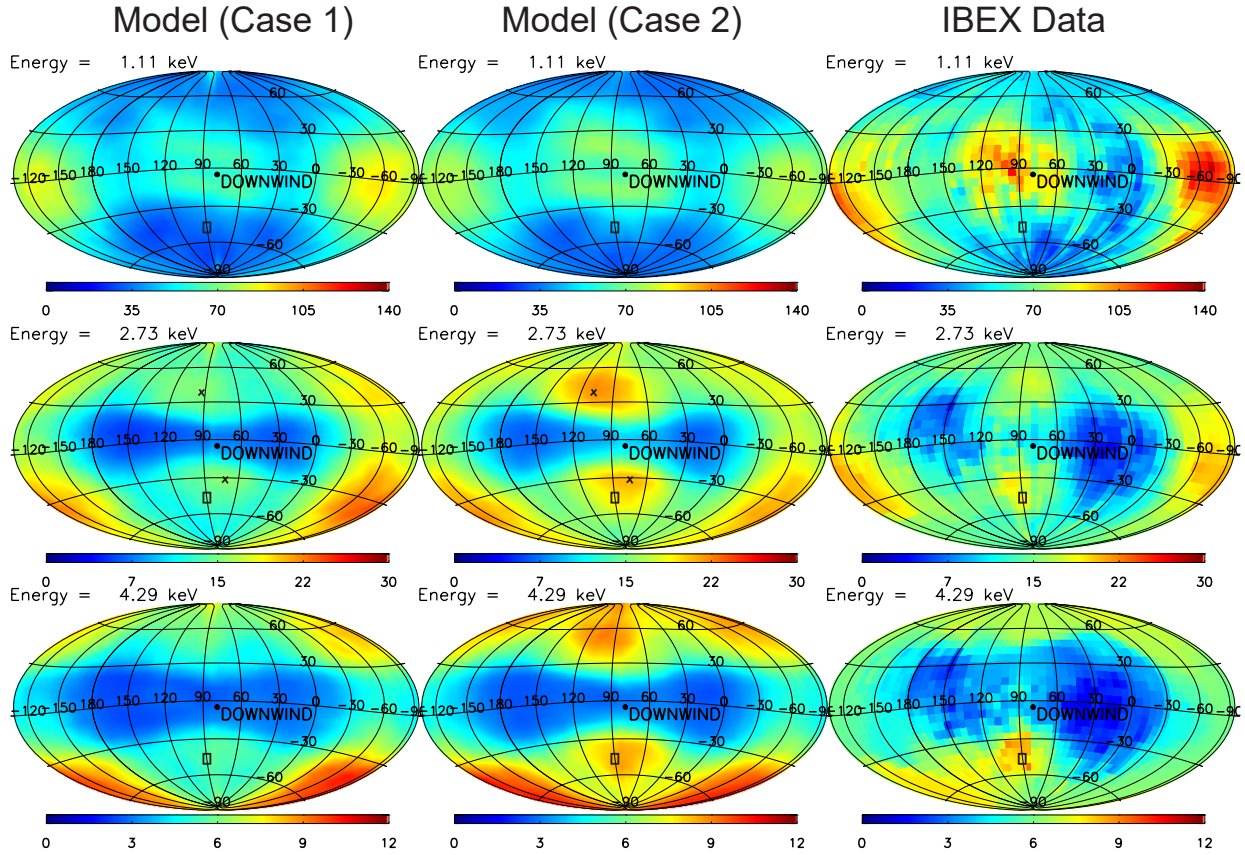


Fig. 2.— ENA sky map of flux centered on the downwind (tail) direction in units of  $(\text{cm}^2 \text{ s sr keV})^{-1}$ . From top to bottom, the energies included are 1.11, 2.73, and 4.29 keV. Left: simulated sky maps for Case 1, which includes latitudinally-varying solar wind without solar magnetic field. Middle: simulated sky maps for Case 2, which includes latitudinally-varying solar wind and solar magnetic field. Right: *IBEX* ENA maps from the first five years (2009-2013) of observations (Schwadron et al. 2014). Simulated sky maps are multiplied by a factor of 1.8. The black box on each map corresponds to the location in the southern lobe where the spectral indices are derived in Table 2. For Case 1 in the 2.73 keV energy band the maximum flux within the lobes are located at  $(\lambda, \beta) = (96^\circ, 42^\circ)$  for the northern lobe and  $(\lambda, \beta) = (72^\circ, -30^\circ)$  for the southern lobe. For Case 2, the northern lobe displays maximum flux at  $(\lambda, \beta) = (108^\circ, 42^\circ)$  and the southern lobe has peak flux centered at  $(\lambda, \beta) = (78^\circ, -30^\circ)$  for the 2.73 keV energy band. The location of maximum flux within the lobes of Cases 1 and 2 are marked by a black ‘x’.

lar wind plasma by the solar magnetic field leads to a temperature enhancement of the plasma. This temperature increase results in a higher ENA flux because higher temperature increases the number of parent ions at higher energies. Therefore, the collimation enhances the number of higher energy parent ions capable of becoming observed ENAs.

Case 2 displays more ENA flux in the high latitude lobes than both Case 1 and the *IBEX* data.

Cases 1 and 2 use the same solar wind conditions at the inner boundary corresponding to the solar minimum and differ only by the inclusion of the solar magnetic field in Case 2. The results replicate a heliosphere that has only experienced solar minimum conditions. Zirnstein et al. (2017) showed the importance of a time dependent solar wind in ENA modeling. Within the heliosheath at high latitudes, there is a mixture of fast and slow so-

lar wind due to the progression of the solar cycle. The structure of the heliosheath and the deflection of slow solar wind from the low latitudes towards the high latitudes also allows for a mixture of slow and fast solar wind at high latitudes independent of the solar cycle. Beyond the deflection of slow wind from lower latitudes (Reisenfeld et al. 2012; Siewert, et al. 2014; Dayeh et al. 2014), there is additional slow wind at the high latitudes during periods of solar maximum due to the latitudinal profile of the solar wind, which further contributes slow wind in the high latitude heliosheath. Because we are not using a time dependent solar wind which includes slow solar wind originating at high latitudes as observed during solar maximum, we overpredict the ENA flux within the high latitude lobes.

We underestimate the ENA flux within the low latitude nose and tail for Cases 1 and 2. In these cases, the solar wind dynamic pressure at 1 AU at the equator is 1.9 nPa. The *IBEX* GDF data presented here is averaged over the years 2009 through 2013. For ENAs observed at the nose, it takes approximately two years from the time the solar wind is observed at 1 AU to cross the termination shock, charge exchange with an interstellar neutral to create an ENA, and then for the ENA to be observed by *IBEX*. In the direction of the nose, *IBEX* is observing ENAs originating from solar wind observed at 1 AU during the years 2007 through 2011. During this time, the solar wind dynamic pressure at 1 AU varied from 2.3 nPa, decreased to 1.2 nPa, and increased again to 2.2 nPa (Figure 1). The thickness of the heliosheath in the heliotail is greater than the thickness in the nose, but the distance over which ENAs are observed is limited by the extinction of parent PUIs. Based on the travel time estimations from Schwadron et al. (2018) and assuming a cooling length of 100 AU in the heliotail, we can approximate the time delay for a 1.1 keV ENA in the tail to be approximately two to eight years. Therefore, *IBEX* is observing in the tail ENAs originating from solar wind observed at 1 AU during the years 2001 through 2011. As noted in Figure 1, with the exception of the end of the year 2003 and the beginning of the year 2004, the dynamic pressure in the year 2008 displayed the lowest dynamic pressure as compared to the seven years preceding it. The dynamic pressure affects the heating of the

solar wind plasma crossing into the heliosheath, which affects ENA production. At the termination shock, the kinetic energy of the solar wind is converted into thermal energy, so a higher dynamic pressure leads to a hotter PUI population. Therefore, our underprediction of ENA flux at the low latitudes may be attributable to our exclusion of a time dependent solar wind, which would account for changes in dynamic pressure.

The underprediction of ENA flux in the low latitude tail could also be attributable to not including the turbulent mixing between the interstellar and solar wind plasma in the tail along reconnected field lines. By not including this region of mixed material between HS and ISM what we call “open heliosheath”, we are limiting our integration distance down the heliotail to where the magnetic field lines are strictly solar. In contrast to the collimated lobes of solar wind plasma in the high latitude tail which extend as far out as 600 AU from the Sun, the region of the low latitude heliotail where the field lines are strictly solar extends to approximately 350 AU in our model. As Kornbleuth et al. (2018) discussed, PUIs within this region of “open heliosheath could be energized due to magnetic reconnection between the solar and interstellar magnetic field, which could possibly lead to an enhancement of ENAs created from this region. While our exclusion of this region could lead to a potential diminishment of ENAs in the low latitude tail, the investigation of this region and its effect on ENAs will be left to a future study.

In Figure 3, we present a comparison of Cases 3 and 4 along with *IBEX* observations. Case 3 reflects the solar magnetic field of solar minimum conditions corresponding to Case 2. Case 4 uses a stronger solar magnetic field corresponding to conditions used in Opher et al. (2015) and Kornbleuth et al. (2018) reproducing a solar magnetic field strength in solar maximum-like conditions. When using a stronger solar magnetic field, the collimation of the solar wind plasma is more pronounced. The additional heating leads to more ENA production. For Cases 1 and 2, the solar wind dynamic pressure is 1.9 nPa at 1 AU. For Cases 3 and 4, the solar wind dynamic pressure is 2.7 nPa at 1 AU. The greater solar wind dynamic pressure in Cases 3 and 4 results in the outward motion of the termination shock, as compared to Cases 1 and 2; how-

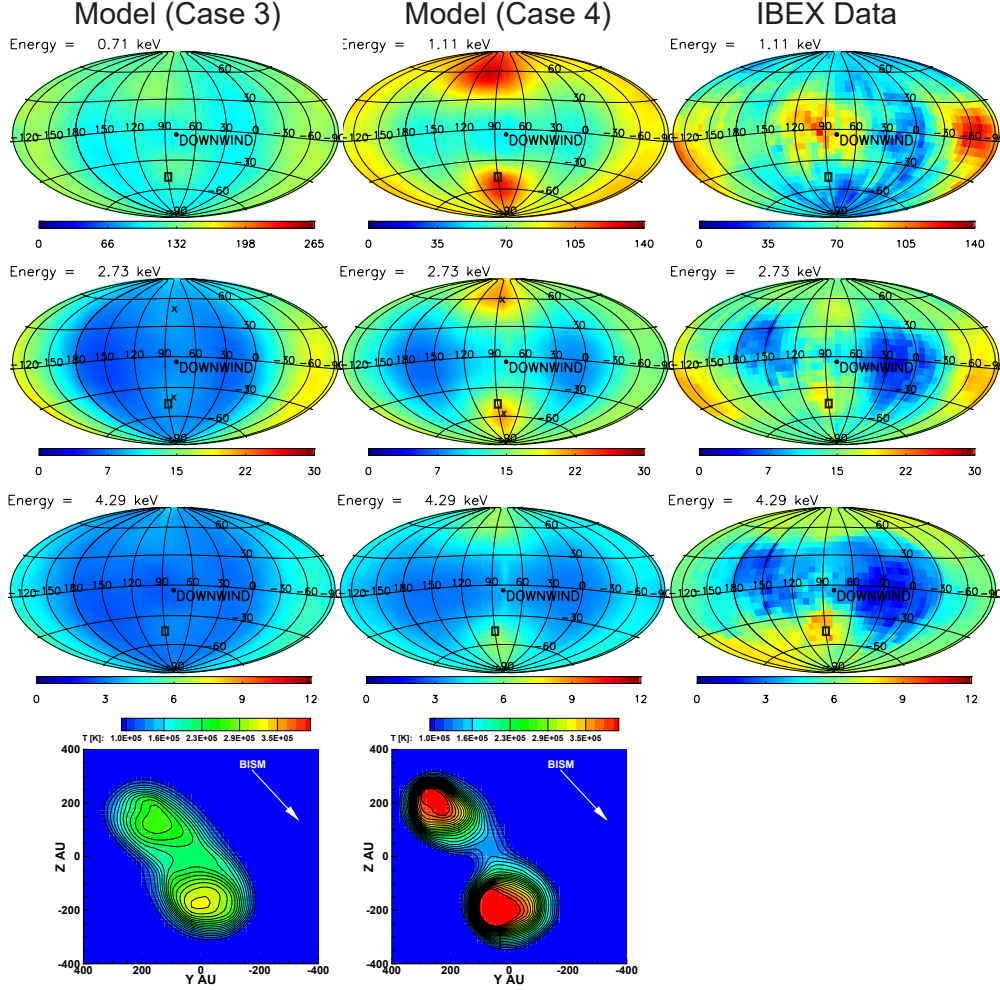


Fig. 3.— ENA sky maps displaying flux in units of  $(\text{cm}^2 \text{ s sr keV})^{-1}$  centered on the downwind (tail) direction. Simulated sky maps for the uniform solar wind model with the radial component of the solar magnetic field, corresponding to the year 2008, set to be 2.94 nT at 1 AU (Case 3, left) and 6.45 nT at 1 AU corresponding to solar maximum-like conditions used in Opher et al. (2015) (Case 4, middle). Also included are *IBEX* ENA maps from the first five years (2009-2013) of observations (Schwadron et al. 2014). Cuts for Case 3 (left) and Case 4 (middle) at  $x = 600$  AU downtail viewed in the direction of ISM flow, with contours and lines of temperature. One can see that the lobes are stronger and exhibit a greater separation along the direction of the interstellar magnetic field in Case 4 than Case 3. Simulated sky maps are multiplied by a factor of 1.8. The black box on each map corresponds to the location in the southern lobe where the spectral indices are derived in Table 2. For Case 3 in the 2.73 keV energy band the maximum flux within the lobes are located at  $(\lambda, \beta) = (84^\circ, 48^\circ)$  for the northern lobe and  $(\lambda, \beta) = (84^\circ, -36^\circ)$  for the southern lobe. For Case 4, the northern lobe displays maximum flux at  $(\lambda, \beta) = (84^\circ, 60^\circ)$  and the southern lobe has peak flux centered at  $(\lambda, \beta) = (84^\circ, -54^\circ)$  for the 2.73 keV energy band. The location of maximum flux within the lobes of Cases 3 and 4 are marked by a black ‘x’.

ever, the greater magnetic field in Case 4 moves the termination shock inward. The increased so-

lar magnetic field strength in Case 4 causes the termination shock to move 6 AU and 27 AU in-



	<i>IBEX</i> Data	Case 1	Case 2	Case 3	Case 4
$\gamma_1$	$1.42 \pm 0.16$	0.64	0.52	1.75	1.49
$\gamma_2$	$1.54 \pm 0.12$	1.73	1.58	2.32	2.39

Table 2: Spectral slopes for *IBEX-Hi* data and Models corresponding to ENA flux modeled through the southern lobe at an ecliptic longitude of  $90^\circ$  and an ecliptic latitude of  $-42^\circ$  (small black box on maps in Figures 2 and 3).  $\gamma_1$  is the spectral slope over the low-energy portion of the spectrum, 0.71-1.74 keV.  $\gamma_2$  is the spectral slope over the high-energy portion of the spectrum, 1.74-4.29 keV.

wards relative to Case 3 in the nose and tail directions, respectively. The closer termination shock results in denser solar wind plasma downstream of the termination shock in all directions, which enhances ENA production. We conclude that the solar magnetic field is responsible for the ENA enhancement in the tail region in Figure 3. While it has been suggested that the structure of the slow and fast solar wind result in the high latitude lobes observed by *IBEX* at energies  $> 2$  keV, our results show that the collimation of the solar wind plasma by the solar magnetic field acts as a critical contributor to the additional ENA flux enhancement and the shape of the observed high latitude lobes.

The maximum flux within the lobes for the 2.73 keV energy band are located at  $(\lambda, \beta) = (84^\circ, 48^\circ)$  for the northern lobe and  $(\lambda, \beta) = (84^\circ, -36^\circ)$  for the southern lobe in Case 3. For Case 4, the northern lobe displays maximum flux at  $(\lambda, \beta) = (84^\circ, 60^\circ)$  and the southern lobe has peak flux centered at  $(\lambda, \beta) = (84^\circ, -54^\circ)$  for the 2.73 keV energy band. Figure 3 also shows cuts down the heliotail at  $x = 600$  AU with contours of temperature. As the solar magnetic field increases, the lobes move to higher latitude. This is seen both in the ENA maps of Figure 3 and the  $x = 600$  AU cuts. This is because the heliospheric jets with a stronger solar magnetic field are more resistant to the pressure from the ISM. We also find in Figure 3 that the lobes in both models are oriented along the direction of the interstellar magnetic field, which is noted for Cases 1 and 2 as well.

In Table 2, we present the spectra for the modeled ENA flux in the southern lobe corresponding to an ecliptic longitude and latitude of  $(\lambda, \beta) = (90^\circ, -42^\circ)$  as compared to *IBEX* data. The location is represented by a black box on the ENA maps in Figures 2 and 3. We only consider the southern lobe because the northern lobe observed by *IBEX* crosses the path of the *IBEX* Ribbon, while the southern lobe does not. The spectral

slope represents how the flux changes as a function of energy for a given latitude and longitude. The flux can be approximated by  $J \propto E^{-\gamma}$ . Previous studies have shown that there is both a low-energy and high-energy component to the polar ENA spectra that comprises two distinct spectral slopes. Dayeh et al. (2011, 2014) examined these two slopes by dividing the spectrum into two portions at 1.74 keV. We divide our spectra in two bins as in Dayeh et al. (2011), with  $\gamma_1$  corresponding to the flux for the 0.71, 1.11, and 1.74 keV energy bands, and  $\gamma_2$  corresponding to the flux for the 1.74, 2.73, and 4.29 keV energy bands. The spectrum of  $\gamma_1$  reflects the signature of the slow solar wind, while  $\gamma_2$  reflects the signature of the fast solar wind.

We find that  $\gamma_1$  is 0.52 and 0.64 for Cases 1 and 2, respectively. These values are considerably lower than what is seen in *IBEX* observations ( $\gamma_1 \sim 1.42 \pm 0.16$ ). As mentioned previously, our model does not include a time dependent solar wind model. As the solar cycle progresses, *IBEX* is observing ENAs produced during both solar minimum and solar maximum conditions. We only are modeling solar minimum conditions and are therefore excluding slow wind at the poles as would be seen during solar maximum, so it is reasonable to expect that we would not be able to reproduce *IBEX* spectra for  $\gamma_1$ . For Cases 3 and 4 we find steeper spectral slopes ( $\gamma_1 \sim 1.75$  and  $\gamma_1 \sim 1.49$ , respectively) than is present in the *IBEX* data, but the spectrum is closer in approximating the *IBEX* data than Cases 1 and 2 due to the slow solar wind.

We find that  $\gamma_2$  is 1.58 and 1.73 for Cases 1 and 2, respectively. Case 2 has a flatter spectrum in the pole, as compared to Case 1, which is a result of the heating caused by the solar wind collimation by the solar magnetic field present in Case 2. Since our poles are populated with fast solar wind due to the solar minimum conditions, we find that

$\gamma_2$  for our model is in good agreement with *IBEX* observations ( $\gamma_2 \sim 1.54 \pm 0.12$ ), with Case 2 having better agreement due to the presence of the solar magnetic field. Cases 3 and 4 have spectra of  $\gamma_2 \sim 2.32$  and  $\gamma_2 \sim 2.39$ , respectively, which yield significantly steeper slopes compared to the *IBEX* data due to the lack of fast solar wind present in the poles for this particular model.

#### 4. Discussion

The “croissant-like” heliosphere with a latitudinally dependent solar wind is able to qualitatively reproduce the *IBEX* maps from the first five years of observations. A more quantitative comparison with a fully time dependent solar wind is left for a future study.

We find that the solar magnetic field plays a critical role in the observed ENA structure. The combination of the slow and fast profile of the solar wind coupled with the collimation of the solar wind plasma by the solar magnetic field leads to the high latitude lobes observed by *IBEX* at energies  $> 2$  keV. As noted in Figure 2, while the latitudinal variation of the solar wind can play a role in the creation of high latitude lobes within the tail, the influence of the solar magnetic field leads to an enhancement of ENA flux within these lobes. This is the first work to explore the effect of the changing solar magnetic field strength on ENA maps.

We predict that the high latitude lobes of strong ENA flux will remain during the course of the solar cycle. As the solar cycle progresses towards solar maximum, the solar wind structure will become more uniform, but the magnitude of the solar magnetic field will increase in strength. Therefore, the collimation of the solar wind plasma by the solar magnetic field strengthens during solar maximum, leading to the persistence of high latitude lobes as shown in Kornbleuth et al. (2018). Our results suggest that the high latitude lobes observed by *IBEX* from 2009 to 2017 (Schwadron et al. 2018) are the result of the collimation of the solar wind plasma by the magnetic field and the increase of the magnetic field during solar maximum.

The authors would like to acknowledge Dr. Nathan Schwadron for supplying information on *IBEX* GDF uncertainties and to acknowl-

edge helpful discussions with Drs. Maher Dayeh and Dan Clemens. This work was supported by NASA Headquarters under the NASA Earth and Space Science Fellowship Program, Grant 80NSSC18K1202. M.O. was partially supported by NASA grant 18-DRIVE18\_2-0029, Our Heliospheric Shield, 80NSSC20K0603. Resources supporting this work were provided by the NASA High-End Computing (HEC) program through the NASA Advanced Supercomputing (NAS) Division at Ames Research Center. The authors would like to thank the staff at NASA Ames Research Center for the use of the Pleiades supercomputer under the award SMD-18-1875. JMS acknowledges support from the Polish National Agency for Academic Exchange (NAWA) Bekker Program Fellowship PPN/BEK/2018/1/00049.

#### REFERENCES

- Lindsay, B. G., & Stebbings, R. F., 2005, *J. Geophys. Res.*, 110, A12213
- Baranov, V. B., & Malama, Y. G. 1993, *J. Geophys. Res.*, 98, 15,
- Dayeh, M. A., McComas, D. J., Livadiotis, G., et al. 2011, *ApJ*, 734, 29
- Dayeh, M. A., Allegrini, F., DeMajistre, R., et al. 2014, *ApJ*, 797, 57
- Dialynas, K., Krimigis, S. M., Mitchell, D. G., Decker, R. B., & Roelof, E. C. 2017, *Nature Astronomy*, 1, 0115,
- Drake, J. F., Swisdak, M., & Opher, M. 2015, *ApJ*, 808, L44
- Funsten, H. O., Allegrini, F., Bochsler, P., et al. 2009, *Space Sci. Rev.*, 146, 75
- Izmodenov, V. V., & Alexashov, D. B. 2015, *ApJS*, 220, 32
- Izmodenov, Vladimir, & Alexashov, Dmitry 2018, *Journal of Physics Conference Series*, 1031, 012014
- Kornbleuth, M., Opher, M., Michael, A. T., & Drake, J. F. 2018, *ApJ*, 865, 84
- Lee, M. A., Fahr, H. J., Kucharek, H., et al. 2009, *Space Sci. Rev.*, 146, 275

- McComas, D. J., Dayeh, M. A., Funsten, H. O., et al. 2019, *ApJ*, 872, 127
- McComas, D. J., Dayeh, M. A., Funsten, H. O., Livadiotis, G., & Schwadron, N. A. 2013, *ApJ*, 771, 77
- McComas, D. J., Allegrini, F., Bochsler, P., et al. 2009, *Space Sci. Rev.*, 146, 11
- McComas, D. J., Dayeh, M. A., Funsten, H. O., et al. 2018, *ApJ*, 856, L10
- Michael, A. T. 2019, PhD Dissertation, Boston University
- Michael, A. T., Opher, M., Provornikova, E., Richardson, J. D., & Tóth, G. 2015, *ApJ*, 803, L6
- Michael, A. T., Opher, M., & Tóth, G. 2018, *ApJ*, 860, 171
- Michael, A. T., Opher, M., Tóth, G., Tennishev, V., & Borovikov, D. 2020, *ApJ*, submitted
- Opher, M., Drake, J. F., Zieger, B., & Gombosi, T. I. 2015, *ApJ*, 800, L28
- Opher, M., Loeb, A., Drake, J., & Toth, G. 2020, *Nature Astronomy*
- Parker, E. N. 1958, *ApJ*, 128, 664
- Parker, E. N. 1961, *ApJ*, 134, 20
- Pogorelov, N. V., Borovikov, S. N., Heerikhuisen, J., & Zhang, M. 2015, *ApJ*, 812, L6
- Ratkiewicz, R., Strumik, M., & Grygorczuk, J., 2012, *ApJ*, 756, 3
- Reisenfeld, D. B., Allegrini, F., Bzowski, M. et al., 2012, *ApJ*, 747,110
- Schwadron, N. A., Moebius, E., Fuselier, S. A., et al. 2014, *ApJS*, 215, 13
- Schwadron, N. A., Allegrini, F., Bzowski, M., et al. 2018, *ApJS*, 239, 1
- Siewert M., Fahr, H. -J., & McComas, D. J., 2014, *A&A*, 565, A81
- Sokół, J. M., Swaczyna, P., Bzowski, M., & Tokumaru, M. 2015, *Sol. Phys.*, 290, 2589
- Sokół, J. M., Bzowski, M., & Tokumaru, M. 2019, *ApJ*, 872, 57
- Tennishev, V., Combi, M., & Davidsson, B. 2008, *ApJ*, 685, 659
- Tokumaru, M., Kojima, M., & Fujiki, K. 2010, *J. Geophys. Res.*, 115, A04102
- Tokumaru, M., Kojima, M., & Fujiki, K. 2012, *J. Geophys. Res.*, 117, A06108
- Tóth, G., van der Holst, B., Sokolov, I. V., et al. 2012, *Journal of Computational Physics*, 231, 870
- Zank, G. P., Heerikhuisen, J., Pogorelov, N. V., Burrows, R., & McComas, D. 2010, *ApJ*, 708, 1092
- Zirnstein, E. J., Funsten, H. O., Heerikhuisen, J., et al. 2016, *ApJ*, 826, 58
- Zirnstein, E. J., Heerikhuisen, J., McComas, D. J., et al. 2018, *ApJ*, 859, 104
- Zirnstein, E. J., Heerikhuisen, J., Zank, G. P., et al. 2017, *ApJ*, 836, 238

---

This 2-column preprint was prepared with the AAS L<sup>A</sup>T<sub>E</sub>X macros v5.2.